IEEE Robotics and Automation Letters (RA-L) paper, presented at ICRA 2026, Vienna, Austria. Cite as RA-L paper.

Design and Optimization of a Samara-Inspired Lightweight Monocopter for Extended Endurance

Xinyu Cai, Shangkun Zhong, Tee Meng Tan, Wei Jun Ang, and Shaohui Foong, *Member, IEEE*

***Abstract*—Small multirotors demonstrate significant potential due to their simple airframe and human-friendly operation. However, the reduced size results in substantially higher energy consumption, which severely limits their flight endurance and restricts their range of applications. Ornithopters, while offering better aerodynamic efficiency, experience energy losses due to the mechanical complexity required to generate reciprocating motion. In this work, inspired by the samara, we present a lightweight aircraft with an exceptionally simple design featuring a single actuator and a mono airfoil. To optimize the flight configuration for minimal power consumption, we employed a Surrogate optimization method that integrates spinning airfoil dynamics, motor-propeller efficiency, and hovering equilibrium. As a result, the proposed vehicle achieves position-controlled hovering flight for up to 26 minutes with a takeoff weight of only 32 grams. Its superior power efficiency is demonstrated by a high power loading of 9.1 grams per watt. Compared to state-of-the-art systems, the proposed design shows significant improvements in both flight endurance and power efficiency. The reliable and stable position-holding flight over an extended period further validates the effectiveness of the proposed methods and the practical applicability of the fabricated prototype.**

***Index Terms*—Aerial systems: Mechanics and control, motion control, biologically-inspired robots.**

I. Introduction

OVER the past few dacades, Micro Aerial Vehicles (MAVs) have attracted growing interest from researchers and engineers, thanks to their compact size, straightforward design, and environmentally friendly operation. Attributed to the advancements in perception [1], actuation [2], as well as locomotion [3], these miniature aerial platforms have achieved remarkable milestones and found widespread application in both civilian and military domains. However, the challenges of achieving sustained flight endurance are exacerbated as the size of the platform is scaled down [4]. For instance, MAVs are constrained by their limited payload capacity, which restricts them to carrying only small batteries, thereby resulting in reduced flight time. Additionally, the decrease in Reynolds numbers significantly diminishes the aerodynamic efficiency of these small aircrafts.

Existing hover-capable centimeter-scale MAVs, such as multirotor, have demonstrated impressive flight autonomy and mission capabilities. However, as the scale decreases, smaller propellers become increasingly power-inefficient due to a rise in Disc Loading (DL), defined as the ratio of thrust to the propeller's disc area. This decline in aerodynamic efficiency significantly limits their flight endurance. Unlike multirotor vehicles that rely on high-speed spinning propellers, ornithopters achieve superior aerodynamic efficiency by leveraging flapping wings [5], [6] and unsteady aerodynamics [7]. Recent advancements have enabled ornithopter platforms to demonstrate mission-capable capabilities, such as hovering [8], agile tracking [9], self-sensing [10], etc. However, generating reciprocating motion at a reduced frequency often requires complex transmission mechanisms, such as gearboxes and crank-rocker systems, which inherently suffer from unavoidable friction and energy losses. As a result, the operational flight time of such small aerial robots is typically limited to a couple of minutes.

A highly underactuated system with minimal actuators can simplify both the mechanical and electronic design of MAVs, reducing takeoff weight while improving flight efficiency. With only one or two actuators, these systems can achieve locomotion capabilities by utilizing passive pitching hinges [11], [12] or balanced mass and inertia distribution [13], [14]. In contrast to relying on direct propulsion from actuators, samara inspired winged self-rotary air vehicles, such as robotic samaras [15] and Single Actuator Monocopters (SAMs) [16], [17], have been developed. The incorporation of a large airfoil enables these designs to feature simpler airframes and lower disc loading, making them an ideal platform for creating lightweight, long-endurance aircraft.

In this work, we aim to develop a lightweight single-actuator monocopter with a focus on maximizing flight endurance. Unlike existing monocopters that emphasize modularity [18], foldability [16], and locomotion performance [19], the proposed robot is built using lightweight components and an optimized flight configuration. As a result, it achieves a takeoff weight of just 32 grams and a remarkable hovering endurance of 26 minutes. To distinguish this work from the previous study in [20] and to highlight its uniqueness and contribution, we emphasize the following:

- This work pushes the design limits of revolving-wing drones to a higher level by employing a minimal number of actuators and airfoils.

Received 7 February 2025; accepted 13 May 2025. Date of publication 30 May 2025; date of current version 9 June 2025. This letter was recommended for publication by Associate Editor I. Maza and Editor G. Loianno upon evaluation of the reviewers' comments. This work was supported by the Ministry of Education, Singapore, through its Academic Research Fund Tier 2 under Grant T2EP50123-0017/MOE-T2EP50123-0004. *(Corresponding author: Shaohui Foong.)*

Xinyu Cai, Tee Meng Tan, Wei Jun Ang, and Shaohui Foong are with the Engineering Product Development Pillar, Singapore University of Technology and Design (SUTD), Singapore 487372 (e-mail: foongshaohui@sutd.edu.sg).

Shangkun Zhong is with the Aviation Key Laboratory of Science and Technology on Flight Control, AVIC Xi'an Automatic Flight Control Research Institute, Xi'an 710065, China.

This article has supplementary downloadable material available at https://doi.org/10.1109/LRA.2025.3575316, provided by the authors.

Digital Object Identifier 10.1109/LRA.2025.3575316

IEEE Robotics and Automation Letters (RA-L) paper, presented at ICRA 2026, Vienna, Austria. Cite as RA-L paper.

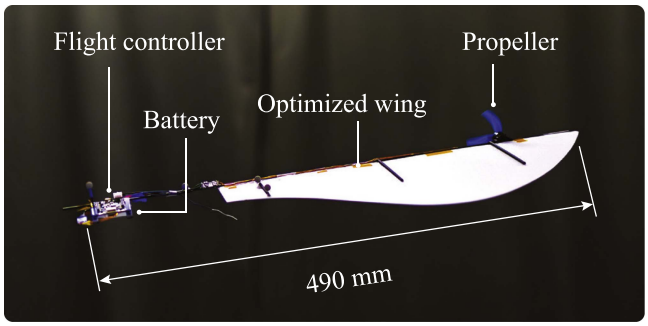

Fig. 1. Proposed hovering-capable aerial vehicle features a lightweight design with an optimized flight configuration, weighing 32 grams and achieving an extended flight time of 26 minutes.

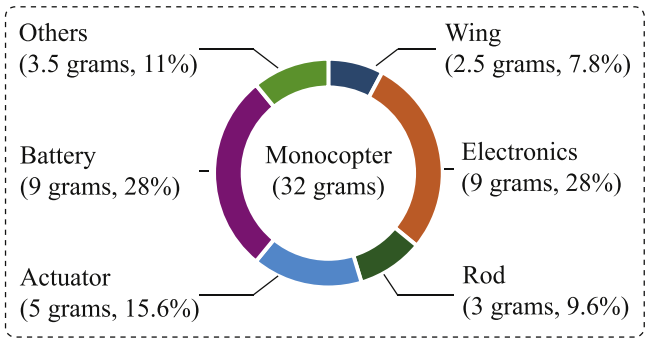

Fig. 2. Weight breakdown of the proposed lightweight monocopter.

- It introduces a more practical optimization strategy for minimizing power consumption in monocopters, incorporating an aerodynamic model of revolving airfoils, a motor–propeller power model under high axial speed, and a hovering equilibrium model.
- It demonstrates benchmark flight performance in terms of both endurance and energy efficiency, outperforming existing hovering-capable MAVs under 100 grams.

II. System Overview

A. Maple Seed Inspired Single Actuator Monocopter

As shown in Fig. 1, the proposed vehicle features a configuration similar to that of a natural maple seed, with its primary mass concentrated on the left side and a large wing profile on the right side. To achieve this configuration, those heavier components such as battery and control circuit are located at right side of the airfoil, resulting a proper Center of Mass (CoM) to enlarge the wing sweeping area. The actuator (motor-propeller) is positioned away from the CoM to create a larger moment arm, enabling it to generate sufficient yaw torque to sustain rapid rotation with relatively low thrust from the propeller. In this way, the proposed monocopter exhibits comparable properties as natural samara seeds [21], allowing its flight attitude to be stabilized using only a single actuator.

However, the reliance on passive attitude stability limits the payload capacity of monocopters, as unexpected payloads can alter the mass and inertia distribution, potentially leading to flight instability or failure. Nevertheless, this does not imply that monocopters lack mission capability. When lightweight payloads are positioned appropriately, their impact on passive stability and flight equilibrium is minimal. Furthermore, treating the additional payload mass as a design variable within the optimization model offers a viable solution for preserving stability while enabling mission execution.

B. Design Highlights

To highlight the key design features and main contributions of the proposed vehicle in this study, we perform a detailed comparison with other benchmark MAVs, as detailed in Table I, including ornithopters, quadrotors, and self-rotating wings. The comparison is emphasized on the following critical aspects:

1) Streamlined Architecture: The proposed vehicle adopts an extremely simple architecture designed to minimize power consumption during flight. As shown in Fig. 2, only the essential components required for flight are utilized. In contrast to vehicles utilizing multiple actuators, the single-actuator platform of the proposed vehicle effectively reduces system complexity and takeoff weight. For instance, minimizing actuator usage significantly reduces energy losses caused by motor and propeller inefficiencies. The large wing profile provides several advantages. On one hand, it enhances aerodynamic efficiency by operating at a lower DL. On the other hand, the samara-like configuration's inherent passive stability allows the robot to remain upright without requiring rapid feedback and active stabilization. Unlike ornithopters that rely on reciprocating motion, the direct use of a motor in the proposed design eliminates the need for complex mechanical systems. This enables the robot to benefit from improved aerodynamics while avoiding the heavy energy losses associated with the drivetrain.

2) Low Power Expenditure: To highlight the flight efficiency of the proposed vehicle, power loading (PL, the ratio of takeoff weight and power consumption) during hovering flights are also included for a comparison to other existing vehicles. With a takeoff weight of 32 grams, the hovering power consumption of the optimized configuration is around 3.5 w, resulting in a PL as high as 9.1 g/w. Comparing to existing prototypes listed in Table I, where the highest efficiency is 8 g/w [20], the proposed robot is markedly higher than other types of vehicles, including multirotors, ornithopters, and self-rotary wings. The result shows that proposed strategies, such as the streamlined architecture and the optimized flight configuration, can effectively reduce the power consumption of the proposed vehicle.

3) Extended Flight Endurance: In addition to using PL to highlight power efficiency, emphasizing flight endurance is more relevant for practical applications. The position-controlled flight endurance test, detailed in Section V, demonstrates that the proposed robot achieves an impressive hover time of 26 minutes with a takeoff weight of 32 grams. Flight endurance comparisons with other state of art, hovering capable MAVs under 100 grams are shown in Table I. Comparing to the benchmark aerial vehicles such as revolving wing drone I in [20] (35.1 grams), the

IEEE Robotics and Automation Letters (RA-L) paper, presented at ICRA 2026, Vienna, Austria. Cite as RA-L paper.

TABLE I
STATE OF ART MAVS UNDER 100 GRAMS WITH HOVERING CAPABILITY

Platforms	Takeoff mass (g)	Flight endurance (minutes)	Number of actuator	Power loading (g/w)	Wingspan (mm)	Year
This work	**32**	**26**	**1**	**9.1**	**722**[a]	**2025**
Revolving-wing drone I [20]	35.1	14.9	2	8	600	2022
Revolving-wing drone II [20]	42.8	21.2	2	7.37	600	2022
Robotic samara-I [15]	75	20	2	-	540[a]	2010
Robotic samara-II [15]	38	10	2	-	360[a]	2010
F-SAM [16]	69	16	1	-	700[a]	2021
DelFly Nimble [9]	28.85	5	4	5	330	2018
Quad-thopter [5]	37.9	9	4	-	280	2018
X-wing ornithopter [6]	27.5	-	4	6.01	280	2018
Crazyflie 2.1+[b]	27	7	4	4.2[c]	47[d]	2014
UMD quadrotor [22]	45	31	4	-	110[c]	2016

[a] The wingspan of the monocopter is defined as twice the distance from the wingtip to the axis of rotation
[b] https://store.bitcraze.io/collections/platforms/products/crazyflie-2-1-plus
[c] From [20]
[d] Propeller diameter

prototype presented in this work (32 grams) demonstrates a significant improvement in flight time, increasing from 14.9 minutes to 26 minutes — an enhancement of approximately 74%. Utilizing geared motors and customized propellers, the UMD (University of Maryland) quadrotor [22] achieves an impressive 31-minute flight time with a 650 mAh battery and a 45-gram takeoff weight. However, while the UMD quadrotor offers about 20% longer endurance than our robot, it operates with 86% higher energy expenditure.

III. SYSTEM MODELING

A. Spinning Airfoil Aerodynamics

Similar to the dynamics of regular propeller, the aerodynamics of a spinning airfoil can also be modeled by using a combination of the blade element theory and momentum theory. At a rotating speed of Ω, the axial thrust (T) and associated torque (Q) about the rotating axis of the robot can be represent as

$$T = C_T\Omega^2, \quad Q = C_Q\Omega^2, \tag{1}$$

where C_T and C_Q are thrust and torque coefficients respectively. Here, we introduce more details of the aerodynamics of the spinning airfoil with momentum theory and blade element theory respectively.

Momentum theory, or the actuator disc theory is based on the conservation of mass, momentum and energy. As shown in Fig. 3(c), $\boldsymbol{V}_i$ is the induced air velocity due to the spinning airfoil, consists of an axial component V_a and a tangential component V_t. The elemental thrust (dT) and torque (dQ) generated by an annular width (dr) at a distance to rotating axis r, can be formulated by using the conservation of momentum as

$$dT = 4\pi r\rho V_a(V_a + V_\infty)dr, \tag{2}$$

$$dQ = 4\pi r^2\rho V_t(V_a + V_\infty)dr, \tag{3}$$

where $\rho = 1.2\ kg/m^3$ is the air density, V_∞ is the freestream axial velocity. However, accurately determining the induced velocity components remains challenging, making it difficult to develop a practical model suitable for optimization purposes.

Unlike the momentum theory, thrust and torque are modeled in terms of induced velocity, the blade element method provide a different solution. For a flat wing surface, the elemental lift force dF_l and drag force dF_d acting on a small segment of width dr can be calculated using its pitching angle β, the chord length c, and the actual air speed V_b observed in its body frame, as expressed in

$$dF_l = \frac{1}{2}\rho C_l V_b^2 c dr, \tag{4}$$

$$dF_d = \frac{1}{2}\rho C_d V_b^2 c dr, \tag{5}$$

where C_l and C_d are the angle of attack (α) related coefficients. The lift force dF_l and drag force dF_d act perpendicular and parallel to the actual air speed V_b. Referring to Fig. 3(d), the lift and drag force can be represented at axial and tangential direction. Then, we have another expression of the thrust and torque generated by the spinning airfoil around its rotating axis, given by

$$dT = dF_l\cos(\epsilon) - dF_d\sin(\epsilon), \tag{6}$$

$$dQ = (dF_l\sin(\epsilon) + dF_d\cos(\epsilon))r, \tag{7}$$

where ϵ is the blade downwash angle, defined as shown in Fig. 3(d). With the geometry relation, we have

$$\epsilon = \beta - \alpha = \arctan\left(\frac{V_a}{V_t - \Omega r}\right). \tag{8}$$

As illustrated by Fig. 3(d), the relation of actual air speed V_b and induced velocity $\boldsymbol{V}_i$ can be wrote as

$$V_b = \sqrt{(\Omega r - V_t)^2 + V_a^2}. \tag{9}$$

IEEE Robotics and Automation Letters (RA-L) paper, presented at ICRA 2026, Vienna, Austria. Cite as RA-L paper.

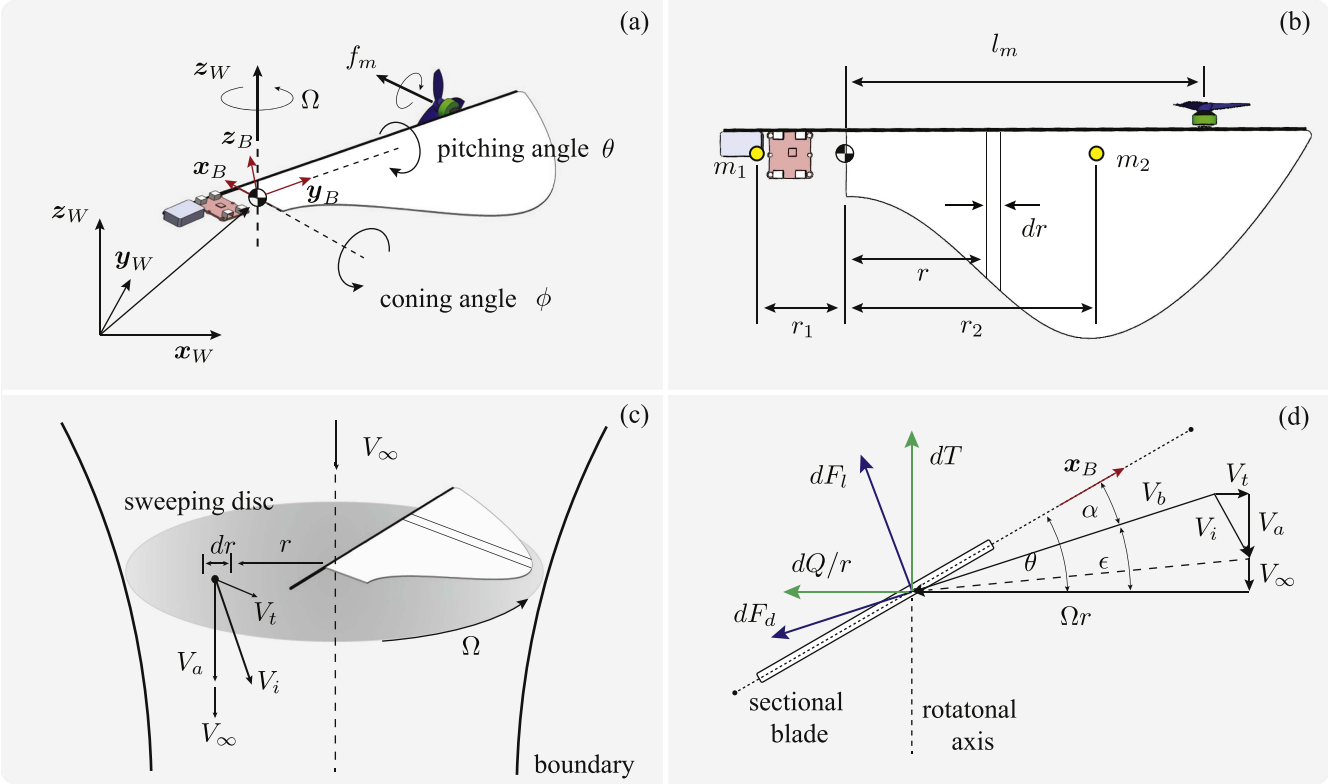

Fig. 3. Combined figure illustrating key concepts and parameters. (a) shows the coordinates in the body frame with definitions of the pitching angle θ and coning angle ϕ. (b) details mass and actuator distribution parameters. (c) illustrates the induced velocity ($\boldsymbol{V}_i$) of an annual element based on momentum theory. (d) depicts the relationship of elemental forces derived from momentum theory (dT, dQ/r) and blade element theory (dF_l, dF_d).

Combining all those above equations, we can obtain the thrust (T) and torque (Q) expression in terms of the pitching angle (β), rotating speed (Ω) as well as the wing geometry (c). With the computed model, we are able to evaluate the thrust and torque coefficient in equation (1) with a particular wing geometry and pitching angle. Considering a static situation with $V_\infty = 0$, and combining (2)–(9), we derive a practical and computational aerodynamic model for spinning wing profile optimization.

B. Propeller Efficiency With High Axial Speed

The propeller operates under distinct conditions in a monocopter compared to other aerial robots, such as quadrotors. Due to its rapid rotation, the propeller experiences a high axial air speed during hovering flights. Consequently, both the thrust and power efficiency are significantly affected. Recalling previous momentum theory based thrust and torque (2) and (3), the induced velocity ($\boldsymbol{V}_i$) caused by the spinning propeller blades is modified due to the high axial air velocity V_∞. As a result, the relationship between other parameters as illustrated in Fig. 3(d) is also influenced. Compared to propellers operating under static conditions, where thrust and torque coefficients remain relatively constant, the coefficients of a propeller exposed to high axial airspeed vary significantly. These variations arise due to changes in the advance ratio and depend on the propeller's aerodynamic profile, rotational speed, and the axial air velocity.

To simplify the analysis, this study focuses on investigating the power consumption (P) of a specific motor-propeller actuator while generating varying levels of thrust (f_m) across a range of axial speeds (V_∞). To this aim, we use a second order polynomial to approximate this relation, as

$$P(f_m, V_\infty) = p_0 + p_1 f_m + p_2 V_\infty + p_3 f_m^2 + p_4 f_m V_\infty + p_5 V_\infty^2, \quad (10)$$

where p_1 - p_5 are the coefficients need to be empirical determined.

C. Relaxed Hovering Solution

Relaxed hovering solution [23] has been widely used to describe the hovering condition for self-spinning aerial robots. In this case, the relaxed hovering equilibrium can be wrote as

$$\int cos(\phi) dT + f_m \sin\theta = mg, \quad (11)$$

$$f_m l_m \cos\theta = \int cos(\phi) dQ, \quad (12)$$

$$(m_1 r_1^2 + m_2 r_2^2)\Omega^2 cos(\phi) sin(\phi) = \int r dT, \quad (13)$$

where ϕ is the coning angle, Ω is the rotating speed, m_1 and m_2 represent the redistributed masses located on the root side and the wing tip side, respectively (as shown in Fig. 3(b)). r_1 and r_2

IEEE Robotics and Automation Letters (RA-L) paper, presented at ICRA 2026, Vienna, Austria. Cite as RA-L paper.

denote their respective distances from the axis of rotation. With a given wing profile and pitching angle, we can calculate the flight equilibrium including rotating speed Ω, coning angle ϕ, and actuator input force f_m, by solving (13)–(15).

IV. Flight Configuration Optimization

A. Parameters Determination

1) Lift and Drag Coefficients: Motivated by modeling of propellers, the aerodynamics of a spinning airfoil can also use a combination of the momentum theory and the blade element theory. Combining the expression of those two methods, we can obtain a computational model to predict the thrust and torque generated by a airfoil with a specified profile, pitching angle, and spinning speed. To this aim, parameters of angle of attached related lift and drag coefficients (C_l and C_d) needed to be earlier determined. Based on previous studies [24] and further verified by [20], the lift and drag coefficients of a airfoil under similar condition can be approximated as

$$C_l(\alpha) = C_{l,0} + C_{l,1} \sin 2\alpha, \tag{14}$$

$$C_d(\alpha) = C_{d,0} + C_{d,1}(1 - \cos 2\alpha), \tag{15}$$

with experimentally identified parameters as $C_{l,0} = 0.13$, $C_{l,1} = 1.67$, $C_{d,0} = 0.046$, $C_{d,1} = 1.14$.

2) Propeller Power Model Under High Axial Speed: The thrust and torque generation model of a propeller at high axial speeds differs significantly from that in a static state. To facilitate the optimization process, we identify the parameters for an empirical model as defined by the previous equation (10). To achieve this, an experimental setup was constructed, consisting of a force/torque (F/T) sensor mounted on a tripod, a servo motor to rotate the actuator at a specified speed, and a circuit designed to drive the actuator and measure instantaneous power consumption. During the test, the actuator is wirelessly controlled using a stepped PWM signal ranging from 0% to 80%. The axial airspeed is generated by the rotation of the actuator, which is positioned 0.2 meters from the axis of rotation. The stepped rotational speed ranges from 0 to 40 $\mathrm{rad/s}$, generating an axial airspeed experienced by the propeller that varies from 0 to 8 $\mathrm{m/s}$.

Details of the results are given by Fig. 4. The plot presents the fitted polynomial model alongside the corresponding measurements. The identified parameters for (10) are obtained as $p_0 = 0.19$, $p_1 = -0.03$, $p_2 = 0.11$, $p_3 = 0.02$, $p_4 = 0.01$, $p_5 = 0.003$, enabling the model to fit the experimental data with a Root Mean Square Error (RMSE) of 0.02 w.

3) Monocopter Configuration: To initiate the optimization process, certain parameters of the monocopter must be predefined. The mass of the vehicle primarily contributed a battery (9-gram), a flight control board (9-gram), and an actuator (5-gram), as detailed in Fig. 2. To maximize the distance between the actuator and the axis of rotation without significantly increasing the footprint, the battery and control board are positioned together near the root of the wing, while the actuator is placed at the wingtip, resulting in $l_m = 250$ mm, (details are shown in Fig. 3(b)). Taking other components into account, including some necessary supporting structures, wing mass, and rod mass

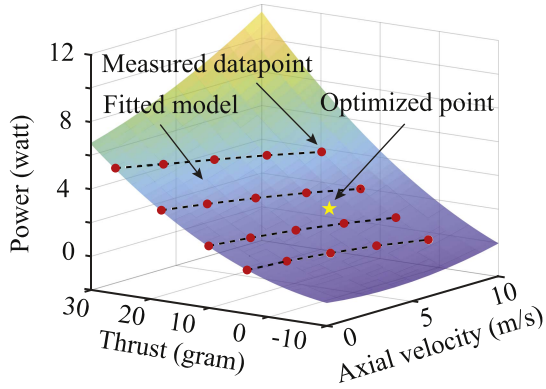

Fig. 4. Power model of the motor-propeller actuator under high axial airspeed is shown, with the colored surface representing the fitted model and the red dots indicating the measured data points. During the test, the airspeed ranges from 0 to 8 m/s, and the motor thrust ranges from 0 to 25 grams. The optimized point is marked with a star, corresponding to an airspeed of 6 m/s, a force of 7.2 grams, and a power of 2.2 w.

for leading edge, the total mass of the vehicle can be approximated using

$$m = \frac{1}{1000}(25 + \rho_{wing} A_{wing} + \rho_{rod} l_{rod}), \tag{16}$$

where $\rho_{wing} = 6.67 \times 10^{-5} \mathrm{g/mm^2}$ is the density of wing material, $\rho_{rod} = 6 \times 10^{-3} \mathrm{g/mm}$ is the density of the rod, A_{wing} is the area of the wing profile in mm^2, l_{rod} is the length of the rod in mm, decided by the wingspan. As shown in 3(b), the mass of the vehicle can also be redistributed around the axis of rotation, as m_1 and m_2 To calculate the flight equilibrium given by equation (11) - (13), those parameters determined by mass distribution are approximated to be $r_1 = 60$ mm, $r_2 = 240$ mm, $m_1 = 20$ grams, $m_2 = 5$ grams.

B. Surrogate Model Based Optimization

Building on the dynamic models introduced in the previous sections, we seek to determine an optimized flight configuration that minimizes power consumption during hovering. The optimization problem can be formulated by

$$\min_{\mathbf{x}} P(\mathbf{x}) = P(\Omega \cos(\theta) l_m, f_m), \tag{17}$$

subject to constraints introduced in previous equations (2) - (13). The decision variable $\mathbf{x}$ including three chord length at different radius to represent the wing profile (c_1 - c_3), pitching angle θ, wingspan length l_w. The proposed objective function seeks to optimize the parameters $\mathbf{x}$ to enable the robot to hover while minimizing power consumption. To achieve this goal, a Surrogate model based optimization method is applied. Detailed process is shown in Fig. 5.

The maximum number of evaluations is set to 1000 to ensure a sufficient search for the optimized solution. The bounds for design variables $\mathbf{x}$ is set as

$$70 \leq c_1, c_2, c_3 \leq 160, \tag{18}$$

$$10 \leq \theta \leq 30, \tag{19}$$

$$300 \leq l_w \leq 400, \tag{20}$$

IEEE Robotics and Automation Letters (RA-L) paper, presented at ICRA 2026, Vienna, Austria. Cite as RA-L paper.

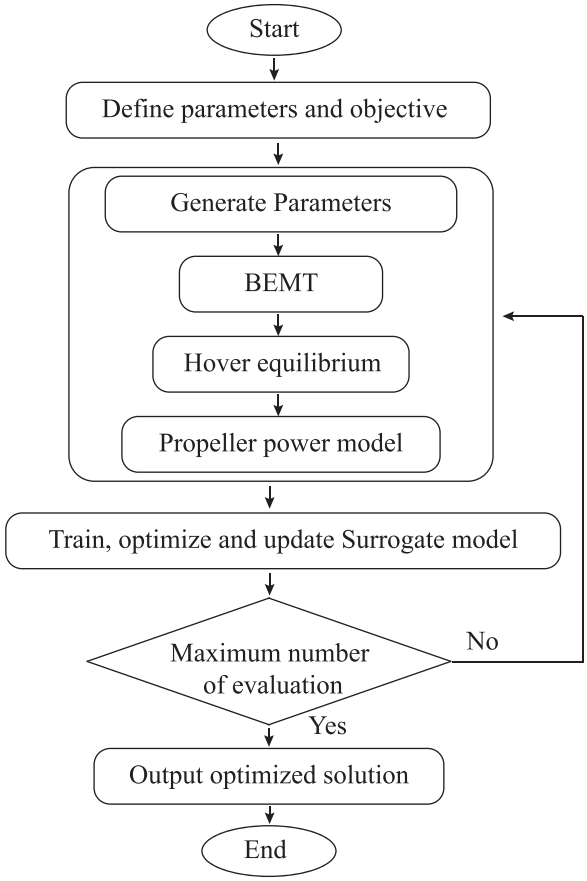

Fig. 5. Detailed steps of the optimization process.

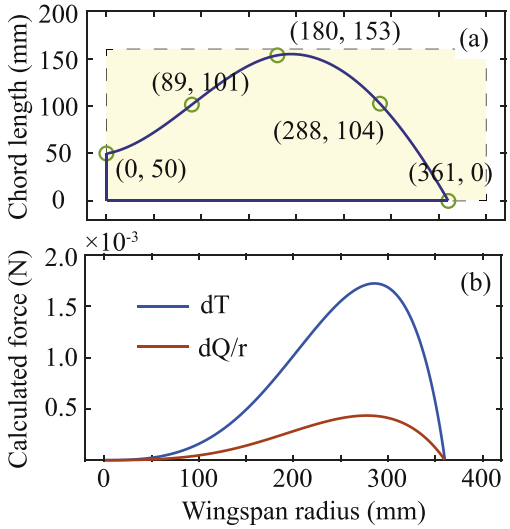

Fig. 6. Details of the optimized wing configuration. (a) shows the wing geometry, where the dashed colored area represents the optimization boundary. (b) depicts the calculated elemental forces based on Blade Momentum Element Theory under the optimized flight equilibrium ($\theta^* = 13.6$ degrees, $\phi^* = 9$ degrees, $\Omega^* = 24$ rds).

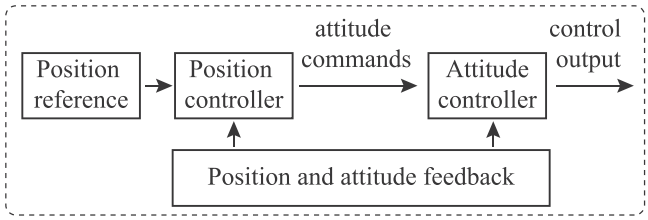

Fig. 7. Diagram illustrates the flight controller implementation. Details of position and attitude controller can be found in [18].

where the chord lengths c_1 to c_3 and wingspan length l_w are measured in mm, while the pitching angle θ is measured in degrees. For the wing profile generation, the radial positions for c_1 - c_3 are chosen to be 25%, 50%, and 80% of l_w, respectively.

C. Optimization Result

The optimization result suggests a wingspan length l_w of 361 mm with chord lengths $c_1 = 101$ mm, $c_2 = 153$ mm, $c_3 = 102$ mm, detailed wing geometry is also shown in Fig. 6(a). The full chord length of the wing shape can also be obtained using the 'spline' function in MATLAB, based on the given and optimized 5 data points shown in Fig. 6(a). Associated with the optimized wing profile, the total mass is calculated to be approximately 29 grams. The optimized pitching angle (θ^*) is approximately 13.6 degrees, resulting in a hovering rate (Ω^*) of 24 $\mathrm{rad/s}$ and a coning angle (ϕ^*) of 9 degrees, as determined by the hovering equilibrium equations (11) - (13). Fig. 6(b) also illustrates the elemental thrust (dT) and torque (scaled by the torque arm, dQ/r) at position r generated by the optimized wing under hovering condition.

In the optimized flight configuration, the predicted motor force f_m is approximately 7.2 grams to hover, resulting in a minimal power consumption of 2.2 watts. The optimized point is also highlighted with a yellow star in Fig. 4.

V. Experiment Evaluation

A. Experimental Vehicle Fabrication

As shown in Fig. 1, the proposed robot primarily consists of a mono-wing, a single actuator, and flight electronics. The entire structure is constructed using a 490 mm, 2 mm × 2 mm carbon rod, chosen for its light weight and rigidity. The airfoil is made from a 1 mm-thick foam sheet, with the optimized geometry precisely cut using a laser cutter. The propulsion is provided by a 1-gram, 2.5-inch, 3-blade propeller, driven by a 4-gram brushless motor (Racerstar, BR1103, 8000KV). A 1-gram ESC is used to accommodate the speed control of the motor. The flight controller chosen is the Crazyfly Bolt (Bitcraze, 7-gram), selected for its lightweight design and ease of deployment. A 1S, 350 mAh LiPo battery (Bitcraze, 9 grams) is used to power the electronics. The other necessary components are custom-designed (Solidworks) and 3D printed (Bambu Lab, X1 - Carbon) with PLA filament. Consequently, the total mass of the fabricated robot is approximately 32 grams, details are listed in Table I.

Unlike other traditional aerial vehicles, the proposed robot relies on asymmetric mass distribution to achieve passive attitude stability. In the design and fabrication of a monocopter,

IEEE Robotics and Automation Letters (RA-L) paper, presented at ICRA 2026, Vienna, Austria. Cite as RA-L paper.

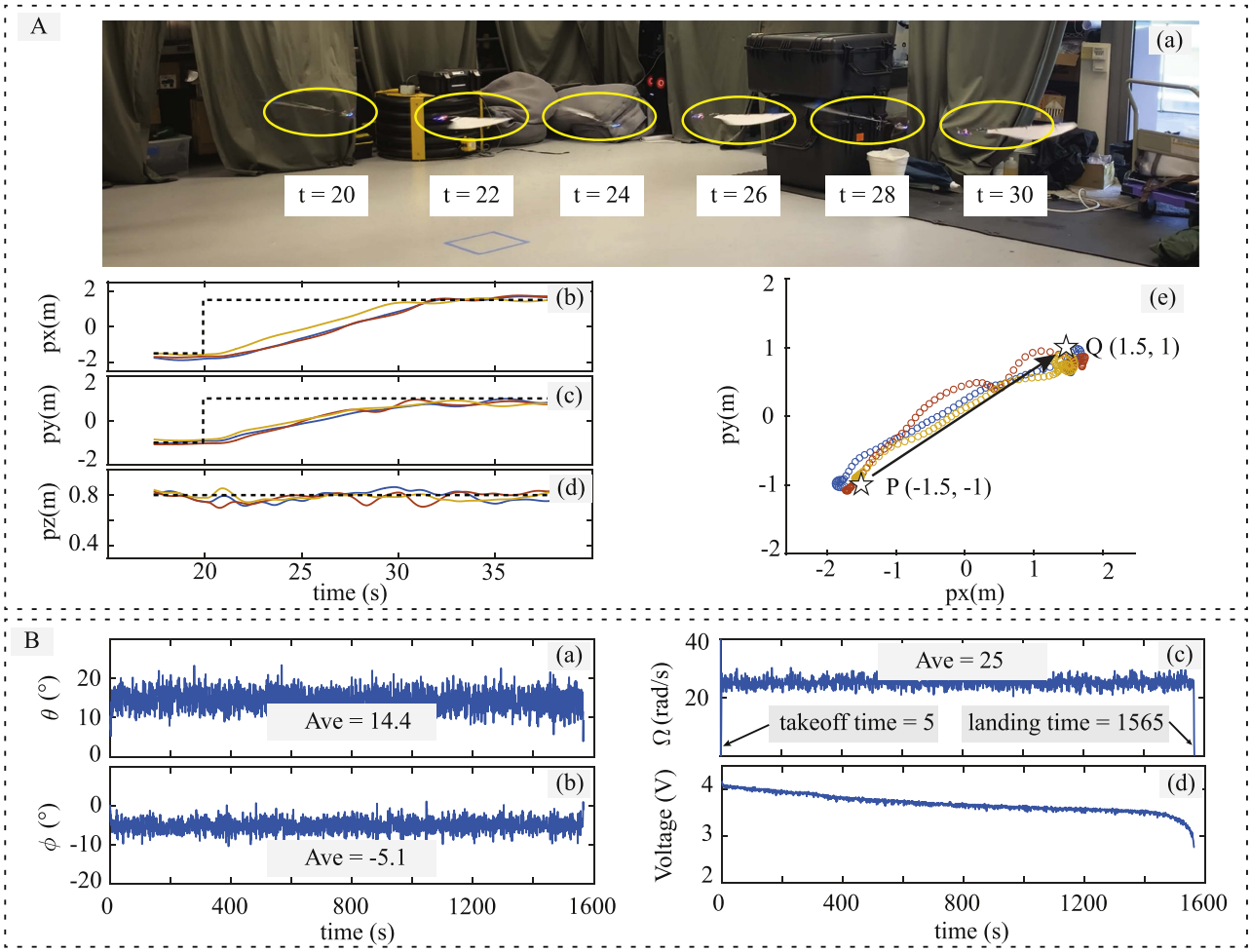

Fig. 8. Panel A illustrates the step-point tracking flights. Plot (a) is a composite image showing the vehicle's movement from point P to Q during a step-point tracking experiment. Plots (b)–(d) present the measured trajectories compared to the reference along the x, y, and z axes, respectively. Plot (e) shows the measured trajectories in the x–y plane across three flight trials. Panel B details the hovering flight. Plots (a)–(c) display the flight attitude: pitching angle, coning angle, and revolving rate, respectively. Plot (d) shows the voltage drop over time.

aside from the aerodynamic optimization of the airfoil, the mass distribution must also be carefully considered. For a single-actuator monocopter without a flapper, the formation of the wing pitching angle is complex and influenced by various factors, including flight configuration, wing geometry, mass and inertia distribution, propeller size, rotational speed of the propeller, and the aerodynamic properties of the airfoil [17]. To achieve a practical hovering configuration closely aligned with the optimization result, particularly the pitching angle θ, the mass distribution is centralized and positioned near the center of mass along the body frame's x-axis. This arrangement ensures an appropriate torque from the centrifugal force to balance the torques generated by the airfoil and propeller precession.

B. Flight Evaluation

1) Experimental Setup: The flight experiments are conducted in an indoor environment equipped with a motion capture system. Using position and attitude feedback from the motion capture system, a control algorithm running on a laptop computes control inputs for the robot in real time to minimize its position errors. The wireless communication between the vehicle and the ground computer is facilitated by Crazyradio (Bitcraze), thanks to its low latency.

To maintain focus, this letter omits the details of the flight controller design. These are available in our previous study [18], which outlines a general strategy for attitude and position stabilization in winged, self-revolving flight configurations, as illustrated in Fig. 7.

2) Step Point Tracking Flights: Step point tracking flights are conducted to show the locomotion ability, as shown in Fig. 8 A. During flights, the robot is commanded to track point Q = [1,5, 1, 0.8], from P = [−1.5, −1, 0.8], with an average traveling speed of 3.6 m/s, details shown in Fig. 8 A. An average position tracking error of 1.03 meters was observed between t = 20 s and 30 s, followed by an average position holding error of 0.13 meters from t = 30 s to 35 s. The stable flights demonstrate that the proposed vehicle maintains its mission capabilities under an optimized flight configuration.

IEEE Robotics and Automation Letters (RA-L) paper, presented at ICRA 2026, Vienna, Austria. Cite as RA-L paper.

3) Hovering Endurance Flights: To assess the flight capability and hovering endurance of the proposed vehicle, we conducted several position-controlled hovering flights with a target altitude of 1.2 meters, details of one flight is shown in Fig. 8 B. Plots (a) and (b) show the attitude during hovering flight, with average values of 14.4 and 5.1 degrees respectively. Plot (c) shows the revolving rate during hovering, with average value of 25 rd/s.

The flight endurance is measured at 1560 seconds (26 minutes), from takeoff to landing, defined as the period during which the altitude fluctuates above and below 0.5 meters. Plot (d) shows the voltage discharge curve over flight duration. Due to the lack of current sensor on the flight controller, the average current and power are measured indirectly, with a value of approximately 0.85 A and 3.5 W respectively, resulting a power loading at 9.1 g/w.

4) Results and Analysis: The measured hovering equilibrium shows only minor deviations from the modeling predictions. Specifically, the measured coning angle ϕ, pitching angle θ, and rotating speed Ω are 5.1 degrees, 14.4 degrees, and 25 rd/s, respectively, while the model predicts values of 9 degrees, 13.6 $^\circ$, and 24 rd/s for these parameters. These discrepancies are likely due to limitations in the modeling assumptions and parameter accuracy.

Additionally, the predicted power consumption differs significantly from the practical value, with modeled and measured values of 2.2 w and 3.5 w, respectively. This discrepancy can be attributed to the following factors: 1) Takeoff mass difference: The modeled takeoff mass is approximately 28 grams, whereas the actual mass in experiments increases to 32 grams. 2) Additional energy requirements: The model predicts power consumption only for takeoff, but in practice, extra energy is required for position corrections during flight. 3) Flight electronics power draw: A notable power expenditure of 0.4 w is measured for the flight electronics. Considering all these factors, the overall model predictions align well with the practical measurements.

VI. Conclusion and Future Work

In this work, we introduced a MAV capable of achieving an extended flight endurance of 26 minutes with a remarkably low takeoff weight of just 32 grams. Taking inspiration from samara seeds, the proposed vehicle exhibits passive attitude stability during flight, enabling an extremely simple structural design that incorporates a single rotor and lightweight components. As a result, our design demonstrates a significant improvement compared to existing benchmark aircraft.

To initialize the optimization process, we use predefined parameters such as a fixed takeoff mass. However, this approach constrains battery selection and overlooks the impact of battery capacity on flight efficiency and endurance. While a heavier battery can extend flight time, it also alters flight equilibrium, potentially deviating from the optimized configuration and leading to a higher disc loading, lower power efficiency. A promising direction for future work is to include battery capacity and discharging model as an optimization variable to more effectively explore its influence on flight performance.

References

[1] G. C. De Croon, J. J. Dupeyroux, C. De Wagter, A. Chatterjee, D. A. Olejnik, and F. Ruffier, "Accommodating unobservability to control flight attitude with optic flow," *Nature*, vol. 610, no. 7932, pp. 485–490, 2022.

[2] S. Kim, Y. -H. Hsiao, Z. Ren, J. Huang, and Y. Chen, "Acrobatics at the insect scale: A durable, precise, and agile micro–aerial robot," *Sci. Robot.*, vol. 10, no. 98, 2025, Art. no. eadp4256.

[3] E. Kaufmann, L. Bauersfeld, A. Loquercio, M. Müller, V. Koltun, and D. Scaramuzza, "Champion-level drone racing using deep reinforcement learning," *Nature*, vol. 620, no. 7976, pp. 982–987, 2023.

[4] D. Floreano and R. J. Wood, "Science, technology and the future of small autonomous drones," *Nature*, vol. 521, no. 7553, pp. 460–466, 2015.

[5] C. De Wagter, M. Karásek, and G. de Croon, "Quad-thopter: Tailless flapping wing robot with four pairs of wings," *Int. J. Micro Air Vehicles*, vol. 10, no. 3, pp. 244–253, 2018.

[6] Y. -W. Chin et al., "Efficient flapping wing drone arrests high-speed flight using post-stall soaring," *Sci. Robot.*, vol. 5, no. 44, 2020, Art. no. eaba2386.

[7] S. P. Sane, "The aerodynamics of insect flight," *J. Exp. Biol.*, vol. 206, no. 23, pp. 4191–4208, 2003.

[8] Z. Tu, F. Fei, J. Zhang, and X. Deng, "An at-scale tailless flapping-wing hummingbird robot. I. Design, optimization, and experimental validation," *IEEE Trans. Robot.*, vol. 36, no. 5, pp. 1511–1525, Oct. 2020.

[9] M. Karásek, F. T. Muijres, C. De Wagter, B. D. Remes, and G. C. De Croon, "A tailless aerial robotic flapper reveals that flies use torque coupling in rapid banked turns," *Science*, vol. 361, no. 6407, pp. 1089–1094, 2018.

[10] S. Fuller, Z. Yu, and Y. P. Talwekar, "A gyroscope-free visual-inertial flight control and wind sensing system for 10-mg robots," *Sci. Robot.*, vol. 7, no. 72, 2022, Art. no. eabq8184.

[11] J. Paulos and M. Yim, "Flight performance of a swashplateless micro air vehicle," in *Proc. 2015 IEEE Int. Conf. Robot. Automat.*, 2015, pp. 5284–5289.

[12] N. Chen et al., "A self-rotating, single-actuated UAV with extended sensor field of view for autonomous navigation," *Sci. Robot.*, vol. 8, no. 76, 2023, Art. no. eade4538.

[13] W. Zhang, M. W. Mueller, and R. D'Andrea, "A controllable flying vehicle with a single moving part," in *Proc. 2016 IEEE Int. Conf. Robot. Automat.*, 2016, pp. 3275–3281.

[14] A. G. Curtis, B. Strong, E. Steager, M. Yim, and M. Rubenstein, "Autonomous 3D position control for a safe single motor micro aerial vehicle," *IEEE Robot. Automat. Lett.*, vol. 8, no. 6, pp. 3566–3573, Jun. 2023.

[15] E. R. Ulrich, D. J. Pines, and J. S. Humbert, "From falling to flying: The path to powered flight of a robotic samara nano air vehicle," *Bioinspiration Biomimetics*, vol. 5, no. 4, 2010, Art. no. 045009.

[16] S. K. H. Win, L. S. T. Win, D. Sufiyan, and S. Foong, "Design and control of the first foldable single-actuator rotary wing micro aerial vehicle," *Bioinspiration Biomimetics*, vol. 16, no. 6, 2021, Art. no. 066019.

[17] X. Cai, S. K. H. Win, L. S. T. Win, D. Sufiyan, and S. Foong, "Cooperative modular single actuator monocopters capable of controlled passive separation," in *Proc. 2022 Int. Conf. Robot. Automat.*, 2022, pp. 1989–1995.

[18] X. Cai, S. K. H. Win, H. Bhardwaj, and S. Foong, "Modeling, control and implementation of adaptive reconfigurable rotary wings (arrows)," *IEEE/ASME Trans. Mechatron.*, vol. 28, no. 4, pp. 2282–2292, Aug. 2023.

[19] E. Tang, W. J. Ang, K. W. Tan, and S. Foong, "Harnessing the differential flatness of monocopter dynamics for the purpose of trajectory tracking in a stable invertible coaxial actuated ROtorcraft (SICARO)," in *Proc. 2024 IEEE Int. Conf. Robot. Automat.*, 2024, pp. 6145–6151.

[20] S. Bai, Q. He, and P. Chirarattananon, "A bioinspired revolving-wing drone with passive attitude stability and efficient hovering flight," *Sci. Robot.*, vol. 7, no. 66, 2022, Art. no. eabg5913.

[21] R. Å. Norberg, "Autorotation, self-stability, and structure of single-winged fruits and seeds (samaras) with comparative remarks on animal flight," *Biol. Rev.*, vol. 48, no. 4, pp. 561–596, 1973.

[22] J. Winslow, M. Benedict, V. Hrishikeshavan, and I. Chopra, "Design, development, and flight testing of a high endurance micro quadrotor helicopter," *Int. J. Micro Air Vehicles*, vol. 8, no. 3, pp. 155–169, 2016.

[23] M. W. Mueller and R. D'Andrea, "Relaxed hover solutions for multicopters: Application to algorithmic redundancy and novel vehicles," *Int. J. Robot. Res.*, vol. 35, no. 8, pp. 873–889, 2016.

[24] D. Lentink and M. H. Dickinson, "Rotational accelerations stabilize leading edge vortices on revolving fly wings," *J. Exp. Biol.*, vol. 212, no. 16, pp. 2705–2719, 2009.